

## Two-photon geometric optics

T. B. Pittman, D. V. Strekalov, D. N. Klyshko,\* M. H. Rubin, A. V. Sergienko, and Y. H. Shih  
*Department of Physics, University of Maryland Baltimore County, Baltimore, Maryland 21228*

(Received 10 October 1995)

We report two-photon correlation experiments using spontaneous parametric down-conversion under a severe manipulation of the input pump field. Considering the case of passing the laser beam through a focusing lens before the down-conversion crystal, theoretical calculations and a series of imaging experiments demonstrate two-photon geometric optics effects. In particular, the imaging in coincidence counts of an aperture placed in one of the down-conversion beams is found to be the analog of a simple spherical mirror system, which displays a “vacuum dispersion” effect in that the object and image distances are wavelength weighted.

PACS number(s): 42.50.Dv, 03.65.Bz

### I. INTRODUCTION

When a laser pump beam is incident on a noncentrosymmetric crystal, the nonlinear process of spontaneous parametric down-conversion (SPDC) of pump photons into pairs of correlated photons may occur [1]. Recently, the inherently quantum mechanical two-photon states produced in SPDC have been used in a number of interesting experiments. The well known correlations [2–4] between the *signal* and *idler* photons constituting a down-converted pair have been cleverly used in a variety of situations ranging from the very practical matter of absolute calibration of single-photon detectors [5–9], to the intuition-challenging studies of photon tunneling time [10] and interaction-free measurement [11]. Furthermore, a variety of two-photon entangled states have been produced by taking advantage of the polarization correlations of the signal and idler photons, as well as the frequency and momentum correlations expressed through the well known phase-matching conditions [1,12]. These entangled states have proved to be an extremely useful experimental source for investigating the concepts of reality and locality found in the Einstein-Podolsky-Rosen (EPR) gedankenexperiment [13]. The convenience of SPDC has led to many experiments (see, for example, [14–22]) concerning tests of Bell’s inequalities [23] and has no doubt influenced the thinking in recent proposals and theoretical papers concerning some of the foundations of quantum mechanics.

There have been numerous other observations of nonclassical states [24–26] and two-photon interference (see, for example, [27–52]) and SPDC has even been proposed and used in the relatively new field of quantum cryptography [53–55]. SPDC has also been found useful in the characterization of optical materials [56], and various communication schemes [57].

In general, most of the above experiments have used pinholes or other means to subselect certain transverse spatial modes of the down-conversion spectrum. Very roughly speaking, in these configurations the SPDC process has been thought of as an intense plane-wave pump input into a

simple “black box” source whose output is two correlated photons in well defined directions. The interesting physics in these setups occurs “down stream,” so to speak, where the photons are manipulated with polarizers, interferometers, detectors, etc. to see the desired effects.

Recently, however, there have been several good studies [58–60] of the spatial distributions of the down-converted photons, and their correlations, with respect to several parameters affecting the interaction *inside* the crystal. In other words, still considering a plane-wave pump input, it is useful to examine the rigorous validity of the phase-matching conditions for various pump spectral widths, crystal lengths, etc. In fact, the transverse spatial coherence properties of the down-converted radiation have been used to observe two-photon physical optics by means of interference and diffraction in the coincidence counting rate when slits are introduced into the down-converted beams [61–63].

Therefore one of the remaining considerations concerning SPDC is what will happen to the correlations of the signal and idler photons if there is a controlled manipulation of the *pump beam*. In this paper, we pass the pump through a focusing lens so that the wave fronts entering the crystal can no longer be taken as plane-wave approximations. Rather, the wave-vector distribution allows the pump to be more accurately thought of as having spherical wave fronts. What we find, through a theoretical model and a series of imaging experiments, is a dramatic restructuring of the momentum correlations that can be interpreted through a simple model based on geometric optics. In particular, we observe two-photon effects that are analogous to standard imaging with a spherical mirror.

The basic idea of the imaging experiment is shown in Fig. 1, which is a topologically equivalent cartoon of the actual experimental setup. The plane wave fronts of the pump beam are weakly focused through the crystal, producing pairs of diverging signal and idler photons. The signal beam travels a distance  $Z_1$  and encounters a detailed aperture in front of a large detector,  $D_1$ . Because it is spatially insensitive, there is no image or shadow of the aperture recorded by  $D_1$ . The idler beam travels a distance  $Z_2$  and is met by a very tiny detector  $D_2$ , which is scanned around in the transverse plane. Therefore, by recording *coincidence counts* as a function of the transverse spatial coordinates of  $D_2$ , we see an image of the aperture placed in the signal beam, even though

\*Permanent address: Quantum Radiophysics Division, Department of Physics, Moscow State University, Moscow 119899, Russia.

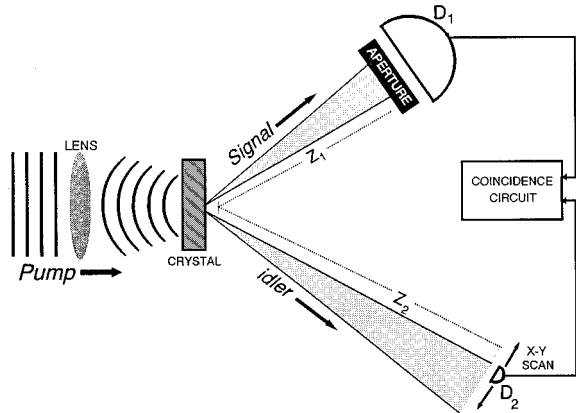


FIG. 1. A topologically equivalent cartoon of the experimental setup. Correlated pairs of signal and idler photons are produced by the SPDC process when an approximately plane-wave pump is focused through a down-conversion crystal. An aperture is placed in front of a large, spatially insensitive detector,  $D_1$ , in the signal beam while a tiny detector,  $D_2$ , is scanned in the transverse plane of the idler beam. By mapping the coincidence counts as a function of the  $x$ - $y$  coordinates of  $D_2$ , an image of the aperture can be seen. Surprisingly, in order to see a sharp image the detector distances  $Z_1$  and  $Z_2$  in the down-conversion beams cannot be arbitrarily chosen, but must obey a two-photon geometric optics relation which is highly dependent on the placement of the lens in front of the crystal.

both detectors' single event counting rates remain constant.

What is most fascinating here is that this imaging process critically depends on the use and placement of the lens. In an earlier paper [64] a similar experiment was performed using a standard plane-wave pump, and a lens placed in the signal beam between the crystal and  $D_1$ . The most interesting feature of that experiment was that in order to see a sharp image in coincidence counts, the various distances between the detectors, the crystal, and the lens had to satisfy a two-photon Gaussian thin lens equation. In particular, the quantum nature of the two-photon state was highlighted by the fact that the placement of  $D_2$  was dictated by the distance of a ray drawn backwards through the lens, reflecting off of the crystal and then forward to  $D_2$ . This effect presented a dramatic example of the original EPR argument in the sense that the momentum entanglement of the two-photon state resulted in a point-by-point transverse plane position correlation to produce a sharp image.

In the present paper, the use of the lens *before the crystal* provides a completely new situation (the idea of this experiment was first discussed in Ref. [65]). In this arrangement, the distances between the detectors and the crystal satisfy a two-photon spherical mirror equation, rather than a Gaussian thin lens equation. Of additional interest is that these prescribed distances are dependent on the wavelengths of the down-converted photons. To demonstrate this dependence, we therefore perform experiments using both the case when the signal and idler wavelengths are equal (the degenerate case) and the case when they are unequal (the nondegenerate case).

## II. THE EXPERIMENT

A schematic of the experimental setup is shown in Fig. 2. A roughly 2 mm diameter pump beam, obtained from the

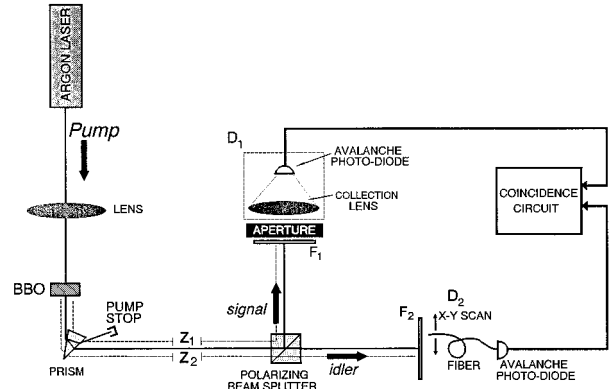


FIG. 2. A schematic of the experimental setup.

351.1 nm line of an argon-ion laser, passes through a plano-convex lens whose focal length is 700 mm. The focused pump wave fronts are then used for the SPDC process in a 3 mm thick nonlinear BBO ( $\beta$ -BaB<sub>2</sub>O<sub>4</sub>) crystal which is placed 100 mm behind the lens. The BBO crystal is cut for a type-II phase matching situation which produces pairs of orthogonally polarized signal (*e*-ray plane of the BBO) and idler (*o*-ray plane of the BBO). Specifically, the optic axis makes an angle  $\psi = 49.2^\circ$  with the center pump direction (the  $z$  direction) which is normal to the input face of the crystal, and the degenerate 702.2 nm wavelength photons of the down-converted pairs emerge collinearly in the  $z$  direction. However, the crystal is mounted on a tilting stage which allows  $\psi$  to be changed. As will be seen, this allows us to demonstrate very interesting quantum effects by creating situations where nondegenerate wavelength photons of a pair emerge from the crystal in the collinear direction.

The UV pump beam is separated from the down-conversion radiation by a fused silica dispersion prism and sent into a beam stop. The remaining signal and idler beams enter a polarizing Glan-Thomson prism which splits each down-conversion pair by reflecting the *e*-ray-polarized signal photons while transmitting the *o*-ray-polarized idlers. The reflected signal photons travel a variable distance and pass through a narrow band filter,  $F_1$ , before encountering detector package  $D_1$ . The total optical distance from the crystal to  $D_1$  is called  $Z_1$ . Meanwhile, the transmitted idler photons travel a variable distance before passing through filter  $F_2$  and hitting detector package  $D_2$ , a distance  $Z_2$  away from the crystal. In actuality, package  $D_1$  is a 2 cm diameter strong collection lens (focal length of 22 mm) which focuses all of the incoming light onto a 0.8 mm diameter dry-ice-cooled avalanche photodiode operating in the Geiger mode. Therefore detector package  $D_1$  can essentially be thought of as a large faced (i.e., 2 cm diameter) single-photon detector which will henceforth be called " $D_1$ ." The aperture to be imaged is placed on the front face of  $D_1$ . Conversely, package  $D_2$  consists of a 0.5 mm diameter multimode fiber whose output is mated with another dry-ice-cooled avalanche photodiode. The input tip of the fiber is scanned in the  $x$ - $y$  transverse plane by two independent encoder drivers each capable of submillimeter steps. Therefore the input tip of the fiber can simply be thought of as a small mobile 0.5 mm diameter detector which will be referred to as " $D_2$ ." The output of

each of the detectors is sent into a coincidence counting circuit with a 1.8 ns acceptance window. In each of the experiments, detector distances  $Z_1$  and  $Z_2$  will be specified, as will the central frequencies of filters  $F_1$  and  $F_2$ .

For any given run of the experiment, the aperture to be imaged in coincidence counts is placed on the front face of detector package  $D_1$ . The shape of the aperture was chosen to be a simple ‘‘unsymmetric cross’’ consisting of two perpendicular equal size bars (roughly  $4.5 \times 1 \text{ mm}^2$ ) that intersect slightly away from their centers. This particular aperture was chosen because it is a very recognizable shape that is easily imaged, while still providing information about its orientation.

### III. THEORY OF THE EXPERIMENT

In general, the experiments presented in this paper produce an image of the aperture placed in the signal beam by mapping the coincidence counting rate as the small detector  $D_2$  is scanned around in the transverse plane of the idler beam. Therefore the aim of this section is to calculate the coincidence counting rate as a function of the transverse spatial parameters involved. We shall see that minimizing this function to obtain the sharpest image results in an equation which dictates the distances between the detectors and the crystal, or, in some sense, a two-photon focal plane location.

#### A. Spherical wave fronts of the pump field inside the crystal

The first step of our analysis is to calculate the classical pump field inside the down-conversion crystal. We assume a standard normal-plane Gaussian intensity distribution of the laser pump beam with a beam waist  $\omega_0$  located some distance on the order of 1 in front of the focusing lens. It is easy to show by the propagation laws of Gaussian beams through thin lenses [66] that the field at the front face of the crystal is

$$E_p(\vec{r}_\perp) = E_p e^{\vec{r}_\perp^2/2\sigma_p^2}, \quad (1)$$

where  $\sigma_p^2 \approx c/\omega_p (d-f-i(\lambda_p/\pi\omega_0^2)f^2)$ . Here  $f$  is the focal length of the lens (700 mm) and  $d$  is the distance between the lens and the front face of the crystal (100 mm).

So inside the crystal the pump field is

$$E_p(\vec{r}_\perp, z, t) = \int d^2k_\perp e^{-i\omega_p t} e^{-i(k_{pz}z + \vec{k}_\perp \cdot \vec{r}_\perp)} \tilde{E}_p(\vec{k}_\perp), \quad (2)$$

where  $k_{pz}$  is the  $z$  component of the pump field, and  $\tilde{E}_p(\vec{k}_\perp)$  is just the Fourier transform of the pump field at the front face of the crystal:

$$\tilde{E}_p(\vec{k}_\perp) = E_p e^{-i\vec{k}_\perp^2 \sigma_p^2/2}. \quad (3)$$

To simplify the integration, we need to extract out the  $\vec{k}_\perp$  dependence in  $k_{pz}$  and introduce a new pump field quantity  $K_p$ , which is defined in Appendix A as the magnitude of the pump  $k$  vector if it were exactly parallel to the  $z$  direction. As is shown in detail in Appendix A, after making the ‘‘thin crystal approximation,’’ the pump field inside the crystal is given by

$$E_p(\vec{r}_\perp, z, t) = E_p' e^{-i(\omega_p t - K_p z)} \int d^2k_\perp e^{-i(\vec{k}_\perp \cdot \vec{r}_\perp + \vec{k}_\perp^2 \sigma_p^2/2)}. \quad (4)$$

Therefore, upon completing the square in the exponent of the integrand and carrying out the Gaussian integration, we find

$$E_p(\vec{r}_\perp, z, t) = E_p'' e^{-i(\omega_p t - K_p z)} e^{i\vec{r}_\perp^2/2\sigma_p^2}. \quad (5)$$

We see that Eq. (5) has the form of a spherical wave, rather than the usual plane-wave model considered in most treatments of SPDC. It is important to note that it is this key difference which will lead to all of the interesting effects in this paper.

#### B. The interaction Hamiltonian and two-photon state

Having a description of the pump field, we may now calculate the interaction Hamiltonian for the type-II SPDC process occurring inside the crystal. The standard form of the Hamiltonian is [67]

$$\mathcal{H}_I = \epsilon_0 \int_V d^3\vec{r} \chi E_p^{(+)} E_o^{(-)} E_e^{(-)} + \text{H.c.}, \quad (6)$$

where  $V$  is the volume of the crystal covered by the classical pump beam  $E_p^{(+)}$ , which is given by Eq. (5), and  $\chi$  is an electric susceptibility tensor which describes the crystal's nonlinearity. The quantized down-conversion field operators inside the crystal are given by

$$E_j^{(-)} = \int_V d^3\vec{k}_j E_j a_{\vec{k}_j}^\dagger e^{-i(k_{jz}z + \vec{k}_j \cdot \vec{r}_\perp - \omega_j t)}, \quad (7)$$

where  $j=o, e$  and  $a_{\vec{k}_j}^\dagger$  is the creation operator for the  $j$ -polarized mode of wave vector  $\vec{k}_j$ . Therefore the Hamiltonian is

$$\begin{aligned} \mathcal{H}_I = & A_1 \int d^3\vec{k}_e \int d^3\vec{k}_o \int_V d^3\vec{r} a_{\vec{k}_o}^\dagger a_{\vec{k}_e}^\dagger \\ & \times e^{i(\omega_e + \omega_o - \omega_p)t} e^{i(k_p - k_e - k_o)z} e^{-i(\vec{k}_e + \vec{k}_o) \cdot \vec{r}_\perp} e^{i/2\sigma_p^2 |\vec{r}_\perp|^2} \\ & + \text{H.c.}, \end{aligned} \quad (8)$$

where H.c. is the Hermitian conjugate and all unimportant constants have been lumped into the factor ‘‘ $A_1$ .’’ We do the volume integration as an area integral times an integral over the crystal length  $L$ , and note that in our experiment the cross sectional area of the crystal is much larger than that of the pump beam. Thus the  $\int d^2r_\perp$  integration is essentially a simple Gaussian over an infinite range, and we obtain

$$\begin{aligned} \mathcal{H}_I = & A_2 \int d^3\vec{k}_e \int d^3\vec{k}_o a_{\vec{k}_o}^\dagger a_{\vec{k}_e}^\dagger e^{i(\omega_e + \omega_o - \omega_p)t} \\ & \times \int_0^L dz e^{i(k_p - k_e - k_o)z} e^{\sigma_p^2/2 (\vec{k}_e + \vec{k}_o)^2} + \text{H.c.} \end{aligned} \quad (9)$$

We can now use the standard technique of first order perturbation theory to describe the output state of the crystal [1]:

$$|\psi\rangle = |0\rangle - \frac{i}{\hbar} \int_{-\infty}^{\infty} dt \mathcal{H}_I |0\rangle. \quad (10)$$

Since we are interested in coincidence counts we can ignore the first term (the vacuum state), and the Hermitian conjugate part which will itself only contribute vacuum. The two-photon part of the output state is thus

$$|\psi\rangle = A_2 \int d^3\vec{k}_e \int d^3\vec{k}_o \delta(\omega_e + \omega_o - \omega_p) \times \int_0^L dz e^{i(k_p - k_{e_z} - k_{o_z})z} e^{\sigma_p^2/2 (\vec{k}_{e_\perp} + \vec{k}_{o_\perp})^2} a_{\vec{k}_o}^\dagger a_{\vec{k}_e}^\dagger |0\rangle. \quad (11)$$

State (11) looks very similar to the usual SPDC two-photon state which results from plane-wave pump input. We see that the time integration has given a  $\delta$  function in frequency which, as usual, leads to the so-called ‘‘frequency phase-matching condition.’’ However, we see that in that part of the state which would usually lead to the momentum ( $k$  vector) phase-matching condition we have a spherical-like term,  $e^{\sigma_p^2/2 (\vec{k}_{e_\perp} + \vec{k}_{o_\perp})^2}$ . It is interesting that, by simply manipulating the pump field by passing it through a lens before the down-conversion crystal, we have redefined the exiting directions that the down-converted photons will follow. As will be seen in the results of the experiments, it is exactly this restructuring of the ordinary momentum phase-matching condition that leads to the interesting effects.

### C. Coincidence counting rate and two-photon amplitude

In order to determine the optimal conditions of our imaging experiment, we need to calculate the coincidence counting rate of the two-photon state (11), subject to a setup similar to that shown in Fig. 2. The average coincidence counting rate is given by the usual Glauber formulation [68,69]:

$$R_c = \lim_{T \rightarrow \infty} \frac{1}{T} \int_0^T dT_1 \int_0^T dT_2 \langle \psi | E_1^{(-)} E_2^{(-)} E_2^{(+)} E_1^{(+)} | \psi \rangle \times S(T_1 - T_2), \quad (12)$$

where the subscripts 1 and 2, respectively, indicate detectors 1 and 2, and  $S(T_1 - T_2)$  is the square pulse coincidence time window function which we take equal to one within a pre-defined value of  $T_1 - T_2$  (usually about 2 ns).

Recall from Fig. 2 that the orthogonally polarized photons of each down-converted pair travel nearly collinearly to a polarizing beam splitter which reflects the e-ray signals to  $D_1$  and transmits the o-ray idlers to  $D_2$ . Thus the free-space field operator at  $D_1$  is

$$E_1^{(+)} = \int d^3\vec{k}'_e E_1 e^{-i\omega_e t_1} e^{i[k'_e Z_1 + \vec{k}'_{e_\perp} \cdot \vec{r}_{e_\perp}]} a_{\vec{k}'_e}, \quad (13)$$

where  $a_{\vec{k}'_e}$  is the annihilation operator of mode  $\vec{k}'_e$ .

Making the paraxial approximation in free space [see appendix A, Eq. (A3)] we have

$$E_1^{(+)} = \int d^3\vec{k}'_e E_1 e^{-i\omega_e T_1} e^{i\vec{k}'_{e_\perp} \cdot \vec{r}_{e_\perp}} e^{-i(|\vec{k}'_{e_\perp}|^2/2\omega_e) c Z_1} a_{\vec{k}'_e}, \quad (14)$$

where  $T_1 \equiv t_1 - Z_1/c$ . Likewise, the field operator at  $D_2$  is

$$E_2^{(+)} = \int d^3\vec{k}'_o E_2 e^{-i\omega_o T_2} e^{i\vec{k}'_{o_\perp} \cdot \vec{r}_{o_\perp}} e^{-i(|\vec{k}'_{o_\perp}|^2/2\omega_o) c Z_2} a_{\vec{k}'_o}. \quad (15)$$

Since we have the usual commutation relations for the normalized creation and annihilation operators:

$$[a_{\vec{k}_j}, a_{\vec{k}'_i}^\dagger] = \delta_{ji} \delta_{\vec{k}\vec{k}'}, \quad (16)$$

it is easy to see that with the two-photon state (11) and operators (14) and (15),

$$\langle \psi | E_1^{(-)} E_2^{(-)} E_2^{(+)} E_1^{(+)} | \psi \rangle = \langle 0 | E_2^{(+)} E_1^{(+)} | \psi \rangle^2 \equiv |A(T_1, T_2)|^2. \quad (17)$$

$|A(T_1, T_2)|^2$  is simply the square of the two-photon probability amplitude. Very interesting physics is manifest in the evaluation of  $|A(T_1, T_2)|^2$ , but the mathematics becomes rather complicated. The calculations are shown in full detail in Appendix B. The end result of the integration in Eq. (17) is

$$|A(T_1, T_2)|^2 = |A_4|^2 \Pi(T_{12}) e^{-1/|X|^2 [\text{Re}(Y)\text{Im}(X) - \text{Im}(Y)\text{Re}(X)]} \quad (18)$$

where  $A_4$  is an unimportant constant, and  $\Pi(T_{12})$  is a rectangular function whose value is one when the difference in detector firing times,  $T_1 - T_2$ , is less than a certain value (typically on the order of 100 fs; see [56] for details) related to the length of the crystal, and zero otherwise. This rectangular function describes the time dependence of the two-photon probability amplitude. Of key importance to our analysis, however, are the quantities  $X$  and  $Y$ , which are functions of the detectors' spatial distances from the crystal:

$$X \equiv Z_1 \frac{c}{\Omega_e} Z_2 \frac{c}{\Omega_o} + \sigma_p^2 \left[ Z_1 \frac{c}{\Omega_e} + Z_2 \frac{c}{\Omega_o} \right],$$

$$Y \equiv (\vec{r}_{e_\perp} - \vec{r}_{o_\perp})^2 \sigma_p^2 + |\vec{r}_{e_\perp}|^2 Z_2 \frac{c}{\Omega_o} + |\vec{r}_{o_\perp}|^2 Z_1 \frac{c}{\Omega_e}, \quad (19)$$

where  $\Omega_o = (2\pi/\lambda_o)c$  and  $\Omega_e = (2\pi/\lambda_e)c$  are the central frequencies of the filters in front of  $D_1$  and  $D_2$ , respectively.

For any given  $T_1$  and  $T_2$ , Eq. (18) gives us an explicit expression of the square of the two-photon probability amplitude as a function of the transverse plane coordinates of the detectors,  $\vec{r}_{o_\perp}$  and  $\vec{r}_{e_\perp}$ . In other words, given some tiny spot in the aperture described by  $\vec{r}_{e_\perp}$ , it essentially describes the regions in space described by  $\vec{r}_{o_\perp}$  where we can obtain a coincidence count. Since we are interested in obtaining the clearest image (in coincidence counts) of the aperture placed in the signal beam, we want the value of this function to be as small as possible. From Eq. (18) it is clear to see that we

have a minimum in the coincident counting rate “spot size” when  $|X|^2$  is a minimum. This gives [see Appendix B, Eq. (B14)]

$$\frac{\lambda_p}{Z_1 \lambda_e} + \frac{\lambda_p}{Z_2 \lambda_o} = \frac{1}{f-d}. \quad (20)$$

Note that this technique is analogous to that used in the standard derivations of simple geometric optics relations, for example, the Gaussian thin lens equation, where minimizing the single beam spot size results in an equation which dictates a focal plane location and various magnification parameters. What we will see from Eq. (20) is that by minimizing the coincidence count rate “spot size” we have derived what can be thought of as a simple “two-photon” spherical mirror geometric optics equation. In other words, given values of  $\lambda_e$  and  $\lambda_o$ , Eq. (20) requires the detectors to be located at specific distances  $Z_1$  and  $Z_2$  in order to have a sharp magnified image.

#### IV. EXPERIMENTAL RESULTS

Equation (20) expresses the key ideas of this paper. Its physical interpretation leaves one with a remarkable impression concerning the quantum nature of the signal and idler photons produced in SPDC. Tests of the predictions of Eq. (20) in two different cases clearly demonstrate what can be called “two-photon geometric optics.” In the first case, the BBO crystal is oriented so that the signal and idler photons which travel through our setup (e.g., in the near collinear direction) have the same wavelength,  $\lambda_e = \lambda_o$ . In the second case, the nondegenerate case is used,  $\lambda_e \neq \lambda_o$ .

##### A. The degenerate case

In this case, the crystal is tilted so that its optic axis makes an angle  $\psi = 49.2^\circ$  with the central pump direction (the  $z$  direction). In this arrangement, one way the ordinary phase-matching conditions [1,12]

$$\omega_p = \omega_e + \omega_o, \quad \vec{k}_p = \vec{k}_e + \vec{k}_o \quad (21)$$

can be satisfied is when the signal and idler photons travel collinearly with the degenerate wavelength of 702.2 nm. This can be seen in the “tuning curve” [1] shown in Fig. 3, which is a plot of the signal (e-ray) and idler (o-ray) wavelengths as a function of the crystal output angles. For a given pump wavelength and angle  $\psi$  the tuning curves can be easily derived from the square of the momentum phase-matching condition of Eqs. (21) and Snell’s law upon exiting the crystal. The tuning curve shown in Fig. 3 is for the planar case, where the optic axis,  $z$  direction, and  $\vec{k}_p$  all lie in the same plane. For the degenerate case experiment, we therefore used identical filters  $F_1$  and  $F_2$  centered at 702.2 nm with bandwidths of about 83 nm, primarily used to cut off the scattered pump radiation. In practice, the size of the pinholes and the aperture itself define the accepted angular spectrum, which is much less than this range, as can be seen from Fig. 3.

Therefore, given that  $\lambda_p = 351.1$  nm, and  $\lambda_e = \lambda_o = 702.2$  nm, we see that Eq. (20), which dictates the clearest image in coincidence counts, reduces to

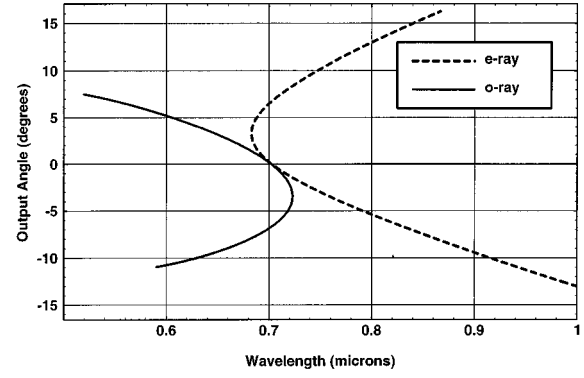


FIG. 3. Tuning curve for type-II SPDC, when the pump beam direction lies along the  $z$  axis, normal to the input face of the crystal. In all of the experiments, the signal and idler wavelengths of interest are those traveling in the nearly collinear direction (e.g., output angle  $\approx 0^\circ$ ). For the case when  $\psi = 49.2^\circ$ , this is the degenerate case  $\lambda_e = \lambda_o = 702.2$  nm.

$$\frac{1}{Z_1} + \frac{1}{Z_2} = \frac{2}{R}, \quad (22)$$

where  $R \equiv f - d = 600$  mm is the approximate radius of curvature of the focused pump wave fronts inside the crystal. Immediately one is struck by the fact that Eq. (22) is the exact analog of the simple spherical mirror equation in ordinary geometric optics. For a given  $Z_1$  (i.e., object distance) and  $R$ , Eq. (22) predicts that a sharp image will be found at  $Z_2$ , and it will be magnified by a factor  $Z_2/Z_1$ .

With the unsymmetric cross aperture placed on the face of  $D_1$ , we tested this prediction by moving  $D_1$  to a distance  $Z_1 = 450$  mm. A sharp image of the aperture was found in coincidence counts when  $D_2$  was scanned in the transverse plane located at a distance  $Z_2 = 900$  mm, the distance at which Eq. (22) is satisfied. The result, shown in Fig. 4, is a density plot of the number of coincidence counts per 20 sec as a function of the idler beam transverse plane coordinates. The data shown are raw data, with each square corresponding to one resting collection location of the 0.5 mm diameter fiber tip of scanning detector  $D_2$ . In other words, it simulates a  $15 \text{ mm}^2$  array of 900 equal sized pixels. The gray-scale shades indicate the number of counts in each location, with the lightest shade corresponding to the maximum number of counts (about 300), while the darker and darker shades correspond to fewer and fewer counts. The darkest shade indicates the background noise of about 40 counts.

The sharp image of the aperture is clearly seen in Fig. 4. Furthermore, note that the length of each of the bars forming the unsymmetric cross is roughly 9 mm, which is the predicted double magnification of the 4.5 mm lengths in the original aperture.

Considering that in this case the idler beam travels twice as far from the crystal as the signal beam, one might be tempted to think that this effect has no dependence on the focusing lens, and is simply a result of the natural linear expansion of the down-converted beams as they propagate away from the crystal. To show that this is not true, we simply remove the lens from our setup and repeat the data collection scan under otherwise identical experimental conditions. The result is shown in Fig. 5. In this completely

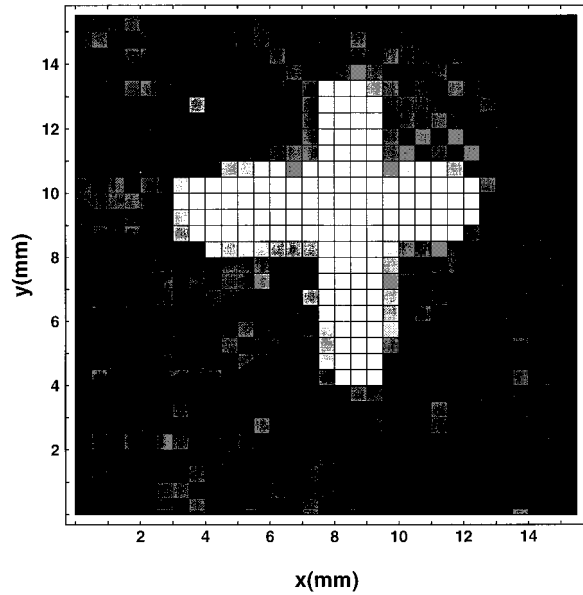


FIG. 4. A map of the coincidence counts as a function of the transverse plane coordinates of  $D_2$ . Each square represents one resting collection location of the 0.5 mm diameter tip of detector  $D_2$ , with the lighter shades corresponding to higher numbers of counts. The size of the bars making up the unsymmetric cross are seen to be about 9 mm, which is the expected magnification factor of 2 predicted from Eq. (22) for the case  $R=600$  mm,  $Z_1 = 450$  mm, and  $Z_2 = 900$  mm. As expected, the orientation of the image was “flipped” from that of the aperture.

“blurred-out” image, the shape of the unsymmetric cross is almost unrecognizable, even though the maximum number of counts is still close to 300. This clearly indicates that the use of a lens in the pump beam imposes a focal planelike condition on the correlations of the down-converted photons.

Although this blurriness in the coincidence count rate image can be predicted by rigorous calculations similar to those

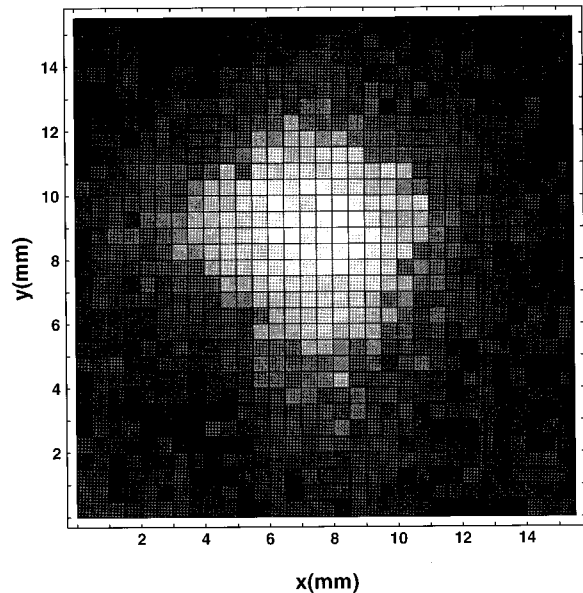


FIG. 5. A repeat of the scan shown in Fig. 4, but with the lens removed from the system.

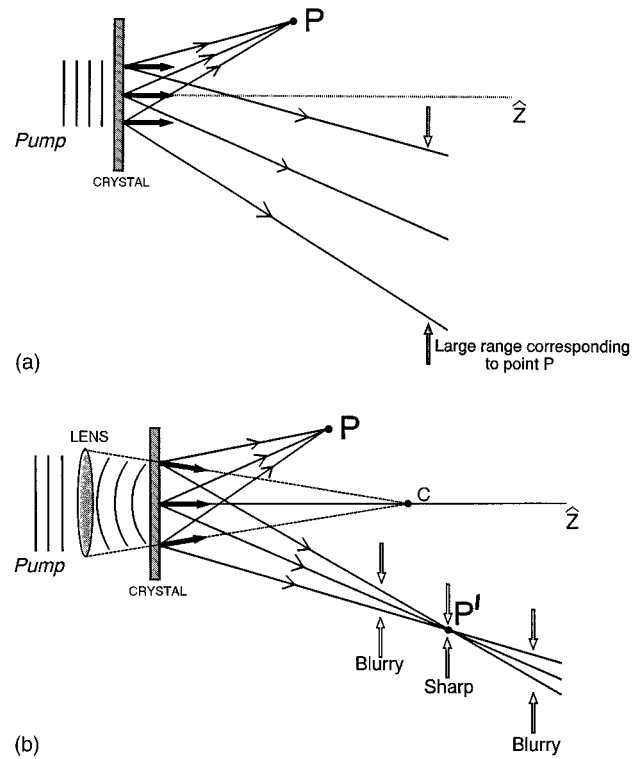


FIG. 6. A cartoon explanation of why a lens before the down-converting crystal results in a sharp image in coincidence counts: (a) without the lens in place, the pump is approximated by plane-wave fronts entering the crystal and for any given point  $P$  in the signal beam, there is a large range in the idler beam which can give coincidence counts. (b) However, when the lens is inserted, the plane pump wave fronts are approximated as spherical, causing a focusing effect to arise in the coincidence counting rate.

above, it is instructive to consider an intuitive picture of the down-conversion processes and their dependence on the lens. We consider the noncollinear topological equivalent of our collinear-beam-and-beam-splitter setup, as discussed in Fig. 1, and indicate the signal and idler photon detection amplitudes by rays pointing in the mode directions. In this nonrigorous model, shown in Fig. 6, the pump beam, distances, and angles are all exaggerated to simply demonstrate the effects.

Since our collinear pinholes and narrow-band detector filters limit the signal and idler wavelengths to a very small range around 702.2 nm, the signal photon and idler photon of any given down-conversion pair emerge from the crystal at equal and opposite angles with respect to the pump direction. This can be seen from the linearity of the tuning curves in Fig. 3 in the region close to 702.2 nm. It can also be seen from the *transverse component* of the  $k$ -vector phase-matching condition [see Eq. (21)] taken in conjunction with Snell’s law upon exiting the crystal:

$$|\vec{k}_e| \sin \alpha_e = |\vec{k}_o| \sin \alpha_o \Rightarrow \omega_e \sin \beta_e = \omega_o \sin \beta_o, \quad (23)$$

where angles  $\alpha$  are inside the crystal and angles  $\beta$  are the exiting angles. From Eq. (23), we see that when  $\omega_o \approx \omega_e$  then  $\beta_o \approx \beta_e$ .

In Fig. 6(a) we examine the case where the lens is removed from the system, and consider the pump to have approximated plane-wave fronts entering the very thin crystal. In this arrangement,  $\vec{k}_p$  is always in the  $z$  direction. Due to the rather large cross sectional area of the pump beam, we see that there are many locations in the transverse plane of the crystal where the down-conversion pair could be “created.” From each of these possible creation points (only three are shown) there is a signal probability amplitude ray which could result in a detection at point  $P$ . The corresponding idler amplitude ray is seen to propagate from the same creation point at the expected equal and opposite angle with respect to  $\vec{k}_p$  at that point; the  $\vec{k}_p$  are indicated by the heavy black arrows. As can be clearly seen, to every point  $P$  in the signal beam there corresponds a large range in the idler beam. Thus in coincidence counts the “image” of point  $P$  is a very large spot, and the “image” of any aperture made up of many such points would be completely blurred out, just like Fig. 5. Although this oversimplified cartoon considers only a very thin crystal, this type of problem becomes even worse when a crystal of any appreciable thickness is used, as has been discussed in several papers [59,60].

However, when a lens is added to the system before the crystal, the approximated plane pump wave fronts which pass through the lens are focused into roughly spherical wave fronts whose radius of curvature is determined by their distance from the focal point of the lens [point  $C$  in of Fig. 6(b)]. Considering the same three possible creation points, we see that the pump wave vectors always point toward the center of curvature, point  $C$ . Again each creation point produces a signal probability amplitude ray which reaches point  $P$ , and the corresponding idler rays exit at an equal and opposite angle with respect to  $\vec{k}_p$  at that creation point. Now, however, these idler rays are seen to *cross at a single point*  $P'$ , rather than diverging as before. The result is a very clear image of point  $P$  in coincidences when the scanning idler beam detector is located at a specific distance from the crystal.

It should be noted that in this ideal scenario it may appear that, in principle, the equal and opposite exit angle requirement of Eq. (23) should not hold. This is due to the fact that the pump wave vectors on the extreme sides of the focused beam no longer make an angle  $\psi = 49.2^\circ$  with the optic axis, and the phase-matching conditions must therefore change. Although this is rigorously true, we emphasize that in practical situations this effect is negligible. Considering the mild focusing of the pump, this change in  $\psi$  is not larger than several mrad, a range for which the tuning curve shown in Fig. 3 does not appreciably change. The end result is that with resolution limited to the order of millimeters by the diameter of  $D_2$ , Fig. 6 provides a somewhat realistic analysis.

In summary this analysis, as well as the rigorous treatment culminating in Eq. (20), indicate that with the lens in place, we establish what can be thought of as a “two-photon focal plane.” The results shown in Figs. 4–6 depict a purely quantum mechanical two-photon phenomenon very reminiscent of ordinary geometric optics. Considering the cartoon topological equivalent of our experiment shown in Fig. 6(b) we see that the imaging behavior in the coincidence counting

rate is exactly the same as one would see if a screen were placed at  $Z_2$  and the avalanche photodiode in  $D_1$  were replaced by a classical pointlike light source, and the down-conversion crystal by a reflecting spherical mirror. For this reason, we refer to Eq. (20) as the “two-photon spherical mirror equation.”

Whereas ordinary simple geometric optics phenomena are conventionally observed on a screen or with a *single* detector, the two-photon geometric optics behavior is observed in *coincidence counts*, revealing its inherently quantum nature. This is yet another example of why the two-photon state produced in SPDC cannot be thought of as simply the product of two individual separated light quanta.

### B. Nondegenerate case

Further interesting tests of the “two-photon spherical mirror equation” can be performed when the signal and idler wavelengths are not equal. In this case, Eq. (20) does not reduce to the simple form of Eq. (22), but

$$\frac{1}{Z_1 \left[ \frac{\lambda_1}{2\lambda_p} \right]} + \frac{1}{Z_2 \left[ \frac{\lambda_2}{2\lambda_p} \right]} = \frac{2}{R}, \quad (24)$$

where  $\lambda_i$  ( $i=1,2$ ) corresponds to the wavelength of the radiation reaching detector  $D_i$ .

In this equation the prescribed object (aperture) and image distances are “wavelength weighted,” and it is clear that the magnification factor is no longer a simple ratio of  $Z_2$  and  $Z_1$ , but the weighted ratio  $M = [(Z_2/Z_1)(\lambda_2/\lambda_1)]$ .

To test this unusual effect, we moved detector  $D_2$  towards the crystal so that  $Z_1 = Z_2 = 450$  mm. So that Eq. (24) was satisfied, we moved the lens further back from the crystal so that  $f - d = R = 450$  mm. As expected, using the degenerate wavelength case to test the system resulted in a sharp unmagnified image. We now imposed the more interesting nondegenerate case by tilting the top of the crystal towards the beam splitter so that  $\psi$ , the angle between the optic axis and the central pump direction, equaled  $45.8^\circ$ . The tuning curve for this pump angle is displayed in Fig. 7(a). It shows that the phase-matching conditions will be satisfied in the collinear direction (i.e., output angle equal to 0) when the signal wavelength is  $\lambda_e = 788$  nm and the idler wavelength is  $\lambda_o = 632$  nm.

We therefore placed a narrow wavelength bandpass filter centered at 788 nm in the signal beam in front of  $D_1$ , and one centered at 632 nm in the idler beam in front of  $D_2$ . The bandpass width of these filters was approximately 2 nm. In this arrangement Eq. (24) is satisfied, and we expect a sharp image with magnification  $M \equiv \lambda_2/\lambda_1 = \lambda_o/\lambda_e = 0.8$ . The result of this data collection scan is shown in Fig. 8. For these data the step size of the scan was reduced from 0.5 mm to 0.25 mm in order to increase the quality of the smaller image. Since the step size was less than the diameter of the fiber tip of  $D_2$ , we can actually attribute some of the perceived blurriness of the image to the overlap (lack of resolution) of the squares in Fig. 8. Nonetheless, we clearly recognize the shape of the unsymmetric cross and observe that the bar length is about 3.6 mm, which is indeed a magnification of 0.8 of the original aperture length.

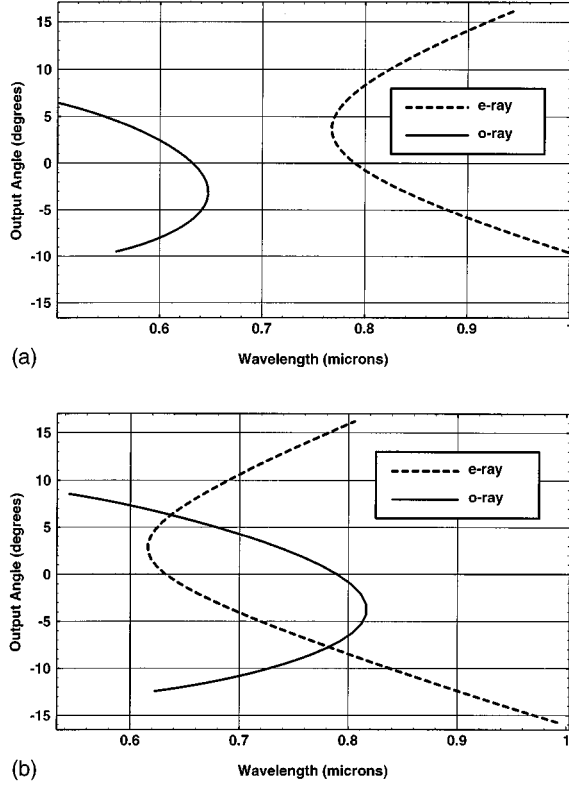


FIG. 7. Tuning curves for the two nondegenerate cases. The crystal is tilted so that (a)  $\psi = 45.8^\circ$ , (b)  $\psi = 52.7^\circ$ . In both cases the fact that the central pump direction is no longer normal to the faces of the crystal causes a distortion of the tuning curves which, in practice, is accommodated by tilting the crystal slightly more (less) to maximize the counting rates.

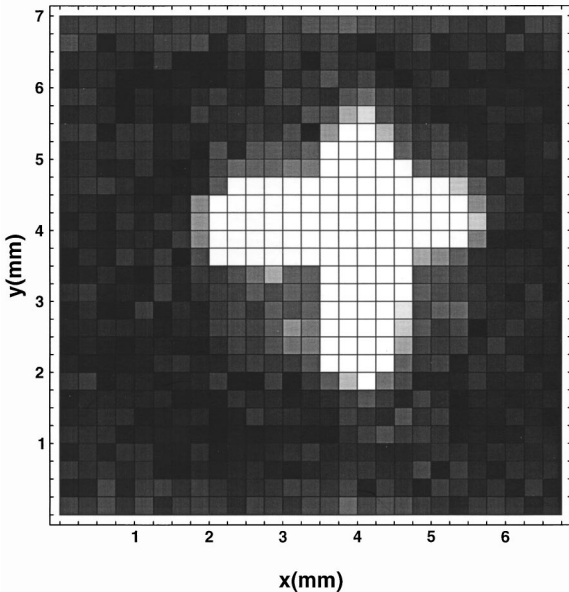


FIG. 8. The nondegenerate case when  $\lambda_e = 788$  nm,  $\lambda_o = 632$  nm, and  $Z_1 = Z_2 = 450$  mm. The weighted behavior of the two-photon spherical mirror equation is manifest as the bar length of about 3.6 mm is the predicted magnification of  $M = [(Z_2/Z_1)(\lambda_o/\lambda_e)] = 0.8$  times the original value.

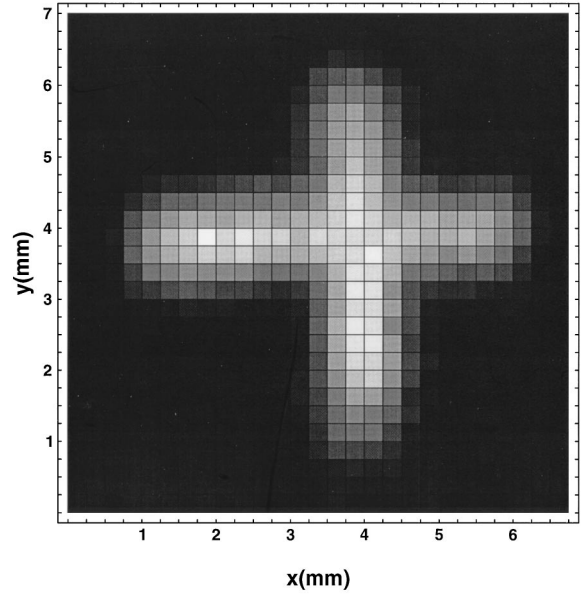


FIG. 9. The nondegenerate case when the wavelengths are switched:  $\lambda_e = 632$  nm,  $\lambda_o = 788$  nm. The magnification value is now  $M = \lambda_o/\lambda_e = 1.25$ .

Because we chose  $Z_1 = Z_2$ , this  $\lambda$ -weighted behavior can be dramatically observed by simply switching the filters in front of the detectors so that the magnification will change from  $\lambda_2/\lambda_1 = \frac{632}{788}$  to  $\lambda_2/\lambda_1 = \frac{788}{632}$ . Since we are using a polarizing beam splitter to increase the coincidence counting rate, we had to change the phase-matching conditions so that the e-ray signal which reaches  $D_1$  has wavelength 632 nm while the o-ray idlers reaching  $D_2$  have wavelength 788 nm. As can be seen in the tuning curve shown in Fig. 7(b), this is accomplished by tilting the crystal in the opposite direction, past the degenerate case configuration, until  $\psi = 52.7^\circ$ . The result of the scan under these conditions is shown in Fig. 9. Again a sharp image is seen, with the bar length roughly equal to 5.6 mm. As expected, this is a magnification factor  $M = \lambda_2/\lambda_1 = 1.25$  of the original aperture's value.

It is very interesting that by simply switching the wavelengths of the down-conversion photons traveling through our system we can dramatically alter the resulting coincidence counting rate image. If one tries to imagine this nondegenerate case in terms of the simple thought model of a spherical reflecting mirror a very curious feature arises: for a given incidence angle of a ray traveling into the mirror from the aperture, the reflected angle is wavelength weighted. Because the optical distances between the detectors and the effective "spherical mirror" are wavelength weighted, one can imagine that the setup experiences some type of "vacuum dispersion." In other words, even though the signal and idler beams actually travel through free space, the imaging behavior and Eq. (24) act as if they were in dispersive media.

## V. CONCLUSIONS

In summary, the use of a lens before the down-converting crystal results in significant alterations of the coincidence counting rate as a function of the transverse spatial coordinates of the detectors. Using the approximately spherical

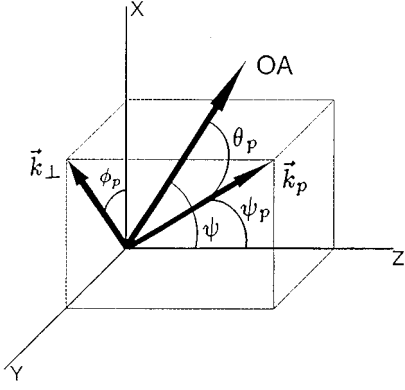


FIG. 10. A representation of the pump wave vector inside the crystal: the optic axis, OA, lies in the  $x$ - $z$  plane making an angle  $\psi$  with the  $z$  axis. In general,  $\vec{k}_p$  does not lie in the  $x$ - $z$  plane, but makes an angle  $\theta_p$  with OA, and an angle  $\psi_p$  with the  $z$  axis.  $\vec{k}_\perp$  is the projection of  $\vec{k}_p$  into the  $x$ - $y$  plane, making an angle  $\phi_p$  with the  $x$  axis. The same conventions hold for the  $e$  ray inside the crystal, as discussed in Appendix B.

pump wave fronts in an otherwise standard field-theoretical calculation of this coincidence counting rate leads to modified wave-number phase-matching conditions and the derivation of the “two-photon spherical mirror equation” [Eq. (20)]. For a given distance between the crystal and  $D_1$  in the signal beam, this equation dictates a location in the idler beam where there is a true point-by-point transverse coordinate position correspondence between the signal and idler photons, which can be considered as an image plane and explained through analogies to simple geometric optics. The two-photon imaging behavior is a direct result of the quantum mechanical correlations of the down-converted photons which, in the spirit of “advanced wave” models (see, for example, Ref. [65]), is seen to be exactly the same as one would observe on a screen placed in the idler beam, if  $D_1$  were replaced by a pointlike light source behind the aperture in the signal beam, and the pump wave fronts inside the crystal were replaced by a spherical mirror. The quantum nature of this situation is highlighted by the fact that the free-space distances required for sharp imaging are dependent on the wavelengths of the down-converted beams.

#### ACKNOWLEDGMENTS

This work is supported by The Office of Naval Research Grant No. N00014-91-J-1430.

#### APPENDIX A

In this appendix, we carry out the integration of the pump field inside the crystal. A schematic of the components of interest of the pump  $k$  vector is shown in Fig. 10.

The input face of the crystal is parallel to the  $x$ - $y$  plane, and the crystal is cut so that the optic axis makes an angle  $\psi$  with the  $z$  axis. The pump wave vector  $\vec{k}_p$  generally does not lie in the  $x$ - $z$  plane but makes an angle  $\psi_p$  with the  $z$ -axis and an angle  $\theta_p$  with the optic axis. Its perpendicular component  $\vec{k}_\perp$  is the projection into the  $x$ - $y$  plane making an angle  $\phi_p$  with the  $x$  axis.

As seen in Eq. (2), the pump field inside the crystal is given by

$$E_p(\vec{r}_\perp, z, t) = \int d^2k_\perp E'_p e^{-i\omega_p t} e^{-i(k_{pz}z + \vec{k}_\perp \cdot \vec{r}_\perp)} e^{-i\vec{k}_\perp^2 \sigma_p^2/2}. \quad (\text{A1})$$

In order to determine the exact  $\vec{k}_\perp$  dependence of  $k_{pz}$ , we note from Fig. 10 that

$$k_{pz} = \sqrt{\left(\frac{\omega_p}{c} n_e(\omega_p, \theta_p)\right)^2 - |\vec{k}_\perp|^2}. \quad (\text{A2})$$

Considering the long focal length and relatively small pump diameter, we are justified in making the paraxial approximation

$$k_{pz} \approx \frac{\omega_p}{c} n_e(\omega_p, \theta_p) - \frac{|\vec{k}_\perp|^2}{2 \frac{\omega_p}{c} n_e(\omega_p, \theta_p)}. \quad (\text{A3})$$

Furthermore, in the paraxial approximation we expand  $k_p$  to first order in  $\theta_p$  about  $\psi$ :

$$\begin{aligned} \frac{\omega_p}{c} n_e(\omega_p, \theta_p) \approx & \frac{\omega_p}{c} \left[ n_e(\omega_p, \psi) \right. \\ & \left. + \frac{d}{d\psi} n_e(\omega_p, \psi) (\theta_p - \psi) + \dots \right] \end{aligned} \quad (\text{A4})$$

and see that Eq. (27) becomes

$$k_{pz} \approx K_p + K_p N_p(\omega_p, \psi) \Delta\theta_p - \frac{|\vec{k}_\perp|^2}{2K_p}, \quad (\text{A5})$$

where  $N_p(\omega_p, \psi) \equiv [1/n_e(\omega_p, \psi)](d/d\psi) n_e(\omega_p, \psi)$  and  $\Delta\theta_p \equiv \theta_p - \psi$ .  $K_p$  is the magnitude of the pump wave vector if it were lying along the  $z$  axis,  $K_p \equiv (\omega_p/c) n_e(\omega_p, \psi)$ . To understand the  $\vec{k}_\perp$  dependence in  $\Delta\theta_p$ , note from the geometry of Fig. 10 that

$$\cos(\theta_p) = \cos(\psi) \cos(\psi_p) + \sin(\psi) \sin(\psi_p) \cos(\phi_p). \quad (\text{A6})$$

Now in the paraxial approximation  $\sin(\psi_p) = |\vec{k}_\perp|/|\vec{k}_p| \approx |\vec{k}_\perp|/K_p \ll 1$  so that

$$\begin{aligned} \cos(\theta_p) \approx & \cos(\psi) \left[ 1 - \frac{1}{2} \frac{|\vec{k}_\perp|^2}{K_p^2} + \dots \right] \\ & + \sin(\psi) \left[ \frac{|\vec{k}_\perp|}{K_p} + \dots \right] \cos(\phi_p). \end{aligned} \quad (\text{A7})$$

But we can also expand  $\cos(\theta_p)$  to first order about  $\psi$ :

$$\cos(\theta_p) \approx \cos(\psi) + \frac{d}{d\psi} \cos(\psi) \Delta\theta_p + \dots \quad (\text{A8})$$

which implies that  $\cos(\theta_p) - \cos(\psi) \approx -\sin(\psi) \Delta\theta_p$ . In comparison with Eq. (31), we find that  $\Delta\theta_p$  is therefore given as

$$\Delta\theta_p \approx \frac{1}{2} \frac{|\vec{k}_\perp|^2}{K_p^2} \cot(\psi) - \frac{|\vec{k}_\perp|}{K_p} \cos(\phi_p) + \dots \quad (\text{A9})$$

Thus, from Eq. (29),

$$\begin{aligned} k_{p_z} &\approx K_p - |\vec{k}_\perp| N_p(\omega_p, \psi) \cos(\phi_p) \\ &= + \frac{|\vec{k}_\perp|^2}{2K_p} [N_p(\omega_p, \psi) \cot(\psi) - 1] \end{aligned} \quad (\text{A10})$$

so that the integral giving  $E_p(\vec{r}_\perp, z, t)$  is

$$\begin{aligned} E_p(\vec{r}_\perp, z, t) &= E'_p e^{-i\omega_p t} \int d^2k_\perp e^{-i[\vec{k}_\perp \cdot \vec{r}_\perp - (\vec{k}_\perp^2 \sigma_p^2/2)]} \\ &\times e^{-i(|\vec{k}_\perp| N_p(\omega_p, \psi) \cos(\phi_p) - |\vec{k}_\perp|^2/2K_p [N_p(\omega_p, \psi) \cot(\psi) - 1])z} \end{aligned} \quad (\text{A11})$$

It is here that we make the “*thin crystal approximation*,” for we see that if  $z$  is small enough we might neglect the computationally troublesome second term of the integrand. For the sake of curiosity, we can get a rough idea of how small the crystal must be to make this approximation rigorously true. We can estimate this value using numbers that are suitable to describe our actual experiment. For example, it is not difficult to evaluate  $N_p(\omega_p, \psi)$  and for a typical pump wavelength of  $\lambda_p = 351.1$  nm and  $\psi \approx 50^\circ$ , we get  $N_p \approx 0.08$ . Furthermore, given the mild focusing of the pump beam we estimate the maximum value of  $\psi_p$  to be about 3 mrad, and estimating  $K_p$  as  $2\pi/\lambda_p$  we get

$$\begin{aligned} |\vec{k}_\perp| N_p(\omega_p, \psi) \cos(\phi_p) &\approx K_p \psi_p N_p(\omega_p, \psi) \cos(\phi_p) \\ &\leq 4000 \text{ m}^{-1}. \end{aligned} \quad (\text{A12})$$

Likewise,

$$\begin{aligned} \frac{|\vec{k}_\perp|^2}{2K_p} [N_p(\omega_p, \psi) \cot(\psi) - 1] &\approx \frac{\psi_p^2 K_p}{2} [N_p(\omega_p, \psi) \cot(\psi) - 1] \\ &\approx 100 \text{ m}^{-1}. \end{aligned} \quad (\text{A13})$$

Therefore, if we assume the crystal is sufficiently thin (e.g., on the order of  $10^{-4}$  m), then the exponent in the second term of the integral is much less than  $\pi$  and we may neglect this term. This thin crystal approximation greatly simplifies the calculations without losing any of the physical insight. Without it, we simply find through numerical calculations that the propagation directions of the down-converted photons inside the crystal (and hence the eventual image magnification) differ slightly in the  $x$  and  $y$  directions. As the crystal gets longer and longer, this “distortion” of the final image becomes more apparent. However, this effect appears to be orders of magnitude smaller than the resolution of our experiment (which is primarily defined by the 0.5 mm diameter of  $D_2$ ), and may be safely neglected. Thus in the thin crystal approximation the pump field inside the crystal is given by

$$E_p(\vec{r}_\perp, z, t) = E'_p e^{-i(\omega_p t - K_p z)} \int d^2k_\perp e^{-i[\vec{k}_\perp \cdot \vec{r}_\perp + (\vec{k}_\perp^2 \sigma_p^2/2)]}. \quad (\text{A14})$$

## APPENDIX B: TWO-PHOTON PROBABILITY AMPLITUDE

In calculating the coincidence counting rate, the form of the mode creation and annihilation operators in the field operators in conjunction with the two-photon state (11) led to the introduction of a two-photon probability amplitude,  $A(T_1, T_2)$ . In this appendix, we perform the integration required to express  $A(T_1, T_2)$  as a simple function of the transverse spatial coordinates. Inserting the field operators and two-photon state into  $\langle 0 | E_2^{(+)} E_1^{(+)} | \psi \rangle$ , we find

$$\begin{aligned} A(T_1, T_2) &= A_2 \int d^3\vec{k}_e \int d^3\vec{k}_o \int_0^L dz \delta(\omega_e + \omega_o - \omega_p) \\ &\times e^{-i\omega_e T_1} e^{-i\omega_o T_2} e^{i(k_p - k_{e_z} - k_{o_z})z} \\ &\times e^{-i(\sigma_p^2/2)(\vec{k}_{e_\perp} + \vec{k}_{o_\perp})^2} e^{i(\vec{k}'_{e_\perp} \cdot \vec{r}_{e_\perp} + \vec{k}'_{o_\perp} \cdot \vec{r}_{o_\perp})} \\ &\times e^{-i|\vec{k}'_{e_\perp}|^2/2\omega_e c Z_1} e^{-i|\vec{k}'_{o_\perp}|^2/2\omega_o c Z_2}. \end{aligned} \quad (\text{B1})$$

Let us assume that we have filters in front of the detectors that only pass a small range of wavelengths and have central frequencies  $\Omega_o$  and  $\Omega_e$  that exactly satisfy the frequency  $\delta$  function in Eq. (B1):

$$\omega_o = \Omega_o + \nu', \quad \omega_e = \Omega_e + \nu, \quad (\text{B2})$$

where  $\nu', \nu \ll \Omega_o, \Omega_e$ ; and  $\Omega_e + \Omega_o = \omega_p$ . Then to do the integration we expand  $k_{e_z}$  and  $k_{o_z}$ , which are inside the crystal, using the paraxial approximations

$$\begin{aligned} k_{o_z} &\approx \frac{\omega_o}{c} n_o(\omega_o) - \frac{|\vec{k}_{o_\perp}|^2}{2\frac{\omega_o}{c} n_o(\omega_o)}, \\ k_{e_z} &\approx \frac{\omega_e}{c} n_e(\omega_e, \theta_e) - \frac{|\vec{k}_{e_\perp}|^2}{2\frac{\omega_e}{c} n_e(\omega_e, \theta_e)}, \end{aligned} \quad (\text{B3})$$

where  $\theta_e$  and all other angles and vectors of subscript  $e$  are defined in exact analogy to the subscript  $p$  vectors and angles in Fig. 10. We can expand  $k_{o_z}$  to first order in  $\nu'$ :

$$k_{o_z} \approx K_o + \frac{\nu'}{u_o} - \frac{|\vec{k}_{o_\perp}|^2}{2K_o}, \quad (\text{B4})$$

where  $K_o \equiv (\Omega_o/c) n_o(\Omega_o)$  and  $u_o^{-1} \equiv d/d\Omega_o [(\Omega_o/c) n_o(\Omega_o)]$  is the inverse of the group velocity.

We first expand  $k_{e_z}$  to first order in  $\theta_e$  about  $\psi$ :

$$k_{e_z} \approx \frac{\omega_e}{c} n_e(\omega_e, \psi) + \frac{\omega_e}{c} n_e(\omega_e, \psi) N_e \Delta\theta_e - \frac{|\vec{k}_{e_\perp}|^2}{2\frac{\omega_e}{c} n_e(\omega_e, \psi)}, \quad (\text{B5})$$

where  $\Delta\theta_e \equiv \theta_p - \psi = \frac{1}{2}\psi_e^2 \cot\psi - \psi_e \cos\phi_e$  in analogy to Eq. (A9). We have defined  $\psi_e \equiv [|\vec{k}_{e\perp}|/(\omega_e/c) n_e(\omega_e, \psi)]$  and  $N_e \equiv [1/n_e(\omega_e, \psi)](d/d\psi) n_e(\omega_e, \psi)$ . We can now expand  $k_{e_z}$  to first order in  $\nu$ :

$$k_{e_z} \approx K_e + \frac{\nu}{u_e} - N_e |\vec{k}_{e\perp}| \cos\phi_e + \frac{|\vec{k}_{e\perp}|^2}{2K_e} (N_e \cot\psi - 1), \quad (\text{B6})$$

where  $K_e \equiv (\Omega_e/c) n_e(\Omega_e, \psi)$  and  $u_e^{-1} \equiv d/d\Omega_e [\Omega_e/c n_e(\Omega_e, \psi)]$ . With these expressions we can now start to evaluate Eq. (B1). Note that  $d^3\vec{k}_e = d^2\vec{k}_{e\perp} dk_{e_z}$ , where to a good approximation  $dk_{e_z} \approx d(\nu/c)$ . Likewise,  $d^3\vec{k}_o \approx d^2\vec{k}_{o\perp} d(\nu'/c)$ . Since  $\delta(\omega_e + \omega_o - \omega_p) = \delta(\nu + \nu')$  the  $\nu'$  integration yields

$$\begin{aligned} A(T_1, T_2) = & A_3 \int d^2\vec{k}_{e\perp} \int d^2\vec{k}_{o\perp} \int d\nu \int_0^L dz e^{-i\nu(T_{12} - Dz)} \\ & \times e^{i(\vec{k}_{e\perp} \cdot \vec{r}_{e\perp} + \vec{k}_{o\perp} \cdot \vec{r}_{o\perp})} e^{i\vec{k}_{e\perp} \cdot N_e \cos\phi_e z} \\ & \times e^{-i[(\Sigma_o^2/2)|\vec{k}_{o\perp}|^2 - (\Sigma_e^2/2)|\vec{k}_{e\perp}|^2 + \sigma_p^2 \vec{k}_{e\perp} \cdot \vec{k}_{o\perp}]}, \quad (\text{B7}) \end{aligned}$$

where  $T_{12} \equiv T_1 - T_2$ ,  $D \equiv 1/u_o - 1/u_e$ , and the  $\Sigma$  are defined as

$$\begin{aligned} \Sigma_o^2 & \equiv \frac{c}{\Omega_o} Z_2 + \sigma_p^2 - \frac{c}{n_o \Omega_o} z, \\ \Sigma_e^2 & \equiv \frac{c}{\Omega_e} Z_1 + \sigma_p^2 - \frac{c}{n_e \Omega_e} (1 - N_e \cot\psi) z. \end{aligned} \quad (\text{B8})$$

But note that in the thin crystal approximation (see Appendix A) the  $z$  dependence in the integrand that depends on  $\vec{k}_{e\perp}$  and  $\vec{k}_{o\perp}$  is negligible. For example, the last term in  $\Sigma_o^2$  is an insignificant fraction of  $\pi$  when multiplied by  $|\vec{k}_{o\perp}|^2$  and may be neglected in the integration. Likewise, the last term in  $\Sigma_e^2$  may also be dropped. Furthermore, estimates of  $e^{i\vec{k}_{e\perp} \cdot N_e \cos\phi_e z}$  show that it may be neglected in the thin crystal approximation. However, considering a typical value of  $D$  is on the order of 0.2 ns/m, we see that for any realistic value of the filter width  $\nu$ , the quantity  $e^{-i\nu Dz}$  is not negligible. Therefore the integral over  $\nu$  and  $z$  yields

$$\int d\nu \int_0^L dz e^{-i\nu(T_{12} - Dz)} = \int_0^L dz \delta(T_{12} - Dz) = \Pi(T_{12}), \quad (\text{B9})$$

where  $\Pi(T_{12})$  is a unit step function which is only different from zero when the difference in detection times,  $T_1 - T_2$ , is between 0 and  $DL$ . Since  $DL$  is essentially the difference in

the amount of time it takes for o-ray and e-ray wave packets to cross the entire down-converting crystal [67],  $\Pi(T_{12})$  basically describes the fact that although the pair of photons can be created anywhere along the length of the crystal with equal probability, they are created at the same time.

The remaining integrals over  $d^2\vec{k}_{o\perp}$  and  $d^2\vec{k}_{e\perp}$  are simply Gaussian and can be evaluated by completing the square in each of the exponents of the integrand. The result is

$$A(T_1, T_2) = A_4 \Pi(T_{12}) e^{i/2 [Y/X]}. \quad (\text{B10})$$

The complex quantities  $X$  and  $Y$  are defined as

$$\begin{aligned} X & \equiv \Sigma_o^2 \Sigma_e^2 - \sigma_p^4 = Z_1 \frac{c}{\Omega_e} Z_2 \frac{c}{\Omega_o} + \sigma_p^2 \left[ Z_1 \frac{c}{\Omega_e} + Z_2 \frac{c}{\Omega_o} \right], \\ Y & \equiv |\vec{r}_{e\perp}|^2 \Sigma_e^2 + |\vec{r}_{o\perp}|^2 \Sigma_o^2 - 2\sigma_p^2 \vec{r}_{e\perp} \cdot \vec{r}_{o\perp} \\ & = (\vec{r}_{e\perp} - \vec{r}_{o\perp})^2 \sigma_p^2 + |\vec{r}_{e\perp}|^2 Z_2 \frac{c}{\Omega_o} + |\vec{r}_{o\perp}|^2 Z_1 \frac{c}{\Omega_e}. \end{aligned} \quad (\text{B11})$$

Therefore

$$|A(T_1, T_2)|^2 = |A_4|^2 \Pi(T_{12}) e^{-Im[Y/X]} \quad (\text{B12})$$

since  $|\Pi(T_{12})|^2 = \Pi(T_{12})$ , and for a general complex number  $\mathcal{Z}$ ,  $|e^{i\mathcal{Z}}|^2 = e^{-2Im\mathcal{Z}}$ . Furthermore, since both  $X$  and  $Y$  are complex,

$$\text{Im}\left[\frac{Y}{X}\right] = \frac{\text{Re}(Y)\text{Im}(X) - \text{Im}(Y)\text{Re}(X)}{\text{Re}(X)^2 + \text{Im}(X)^2}. \quad (\text{B13})$$

However, since  $\sigma_p^2 \approx c/\omega_p [d - f - i(\lambda_p/\pi\omega_0^2)f^2]$  we see from Eq. (B11) that

$$\text{Re}(X) = \left[ \frac{Z_1 \lambda_e}{\lambda_p} \frac{Z_2 \lambda_o}{\lambda_p} + (d - f) \left( \frac{Z_1 \lambda_e}{\lambda_p} + \frac{Z_2 \lambda_o}{\lambda_p} \right) \right] \left[ \frac{\lambda_p}{2\pi} \right]^2 \quad (\text{B14})$$

since  $c/\Omega_j = \lambda_j/2\pi$ . Meanwhile, the imaginary part of  $X$  is

$$\text{Im}(X) = \frac{-c}{\omega_p} \frac{\lambda_p f^2}{\pi \omega_0^2} \left[ \frac{Z_1 \lambda_e}{2\pi} + \frac{Z_2 \lambda_o}{2\pi} \right]. \quad (\text{B15})$$

So for any standard choice of the experimental parameters,  $\text{Im}(X) \ll \text{Re}(X)$ . Therefore the final evaluation of the square of the two-photon probability amplitude gives

$$\begin{aligned} |A(T_1, T_2)|^2 & \approx |A_4|^2 \Pi(T_{12}) e^{-[1/\text{Re}(X)^2][\text{Re}(Y)\text{Im}(X) - \text{Im}(Y)\text{Re}(X)]}, \end{aligned} \quad (\text{B16})$$

which is a minimum when  $\text{Re}(X)^2 = 0$ .

- [1] D.N. Klyshko, *Photons and Non-linear Optics* (Gordon and Breach Science, New York, 1988).  
 [2] D.C. Burnham and D.L. Weinberg, Phys. Rev. Lett. **25**, 84 (1970).

- [3] S. Friberg, C.K. Hong, and L. Mandel, Phys. Rev. Lett. **54**, 2011 (1985).  
 [4] I. Abram, R.K. Raj, J.L. Oudar, and G. Dolique, Phys. Rev. Lett. **57**, 2516 (1986).

- [5] A.A. Malygin, A.N. Penin, and A.V. Sergienko, *Pis'ma Zh. Eksp. Teor. Fiz.* **33**, 493 (1981) [*JETP Lett.* **33**, 477 (1981)].
- [6] J.G. Rarity, K.D. Ridley, and P.R. Tapster, *Appl. Opt.* **26**, 4616 (1987).
- [7] A.N. Penin and A.V. Sergienko, *Appl. Opt.* **30**, 3582 (1991).
- [8] P.G. Kwiat, A.M. Steinberg, R.Y. Chiao, P.H. Eberhard, and M.D. Petroff, *Phys. Rev. A* **48**, 867 (1993).
- [9] P.G. Kwiat, A.M. Steinberg, R.Y. Chiao, P.H. Eberhard, and M.D. Petroff, *Appl. Opt.* **33**, 1844 (1994).
- [10] A.M. Steinberg, P.G. Kwiat, and R.Y. Chiao, *Phys. Rev. Lett.* **71**, 708 (1993).
- [11] P.G. Kwiat, H. Weinfurter, T. Herzog, and A. Zeilinger, *Phys. Rev. Lett.* **74**, 4763 (1995).
- [12] A. Yariv, *Quantum Electronics* (John Wiley and Sons, New York, 1985).
- [13] A. Einstein, B. Podolsky, and N. Rosen, *Phys. Rev.* **35**, 777 (1935).
- [14] Y.H. Shih and C.O. Alley, *Phys. Rev. Lett.* **61**, 2921 (1988).
- [15] J.G. Rarity and P.R. Tapster, *Phys. Rev. A* **41**, 5139 (1990).
- [16] J.G. Rarity and P.R. Tapster, *Phys. Rev. Lett.* **64**, 2495 (1990).
- [17] J.D. Franson, *Phys. Rev. A* **44**, 4552 (1991).
- [18] J. Brendel, E. Mohler, and W. Martienssen, *Europhys. Lett.* **20**, 575 (1992).
- [19] P.G. Kwiat, A.M. Steinberg, and R.Y. Chiao, *Phys. Rev. A* **47**, 2472 (1993).
- [20] T.E. Kiess, Y.H. Shih, A.V. Sergienko, and C.O. Alley, *Phys. Rev. Lett.* **71**, 3893 (1993).
- [21] T.B. Pittman, Y.H. Shih, A.V. Sergienko, and M.H. Rubin, *Phys. Rev. A* **51**, 3495 (1995).
- [22] J.R. Torgerson, D. Branning, C.H. Monken, and L. Mandel, *Phys. Rev. A* **51**, 4400 (1995).
- [23] J.S. Bell, *Physics* **1**, 195 (1964).
- [24] C.K. Hong and L. Mandel, *Phys. Rev. Lett.* **56**, 58 (1986).
- [25] J.G. Rarity, P.R. Tapster, and E. Jakeman, *Opt. Commun.* **62**, 201 (1987).
- [26] P.G. Kwiat and R.Y. Chiao, *Phys. Rev. Lett.* **66**, 588 (1991).
- [27] R. Ghosh and L. Mandel, *Phys. Rev. Lett.* **59**, 1903 (1987).
- [28] C.K. Hong, Z.Y. Ou, and L. Mandel, *Phys. Rev. Lett.* **59**, 2044 (1987).
- [29] Z.Y. Ou and L. Mandel, *Phys. Rev. Lett.* **61**, 50 (1988); **61**, 54 (1988).
- [30] J.G. Rarity, P.R. Tapster, E. Jakeman, T. Larchuk, R.A. Campos, M.C. Teich, and B.E.A. Saleh, *Phys. Rev. Lett.* **65**, 13 481 (1990).
- [31] Z.Y. Ou, L.J. Wang, X.Y. Zou, and L. Mandel, *Phys. Rev. Lett.* **41**, 566 (1990).
- [32] P.G. Kwiat, W.A. Vareka, C.K. Hong, H. Nathel, and R.Y. Chiao, *Phys. Rev. A* **41**, 2910 (1990).
- [33] Z.Y. Ou, X.Y. Zou, L.J. Wang, and L. Mandel, *Phys. Rev. Lett.* **65**, 321 (1990).
- [34] Z.Y. Ou, X.Y. Zou, L.J. Wang, and L. Mandel, *Phys. Rev. A* **42**, 2957 (1990).
- [35] L.J. Wang, X.Y. Zou, and L. Mandel, *Phys. Rev. Lett.* **66**, 1111 (1991).
- [36] X.Y. Zou, L.J. Wang, and L. Mandel, *Phys. Rev. Lett.* **67**, 318 (1991).
- [37] J. Brendel, E. Mohler, and W. Martienssen, *Phys. Rev. Lett.* **66**, 1142 (1991).
- [38] J.G. Rarity and P.R. Tapster, *Phys. Rev. A* **45**, 2052 (1992).
- [39] A.M. Steinberg, P.G. Kwiat, and R.Y. Chiao, *Phys. Rev. Lett.* **68**, 2421 (1992).
- [40] X.Y. Zou, T. Grayson, L.J. Wang, and L. Mandel, *Phys. Rev. Lett.* **68**, 3667 (1992).
- [41] P.G. Kwiat, A.M. Steinberg, and R.Y. Chiao, *Phys. Rev. A* **45**, 7729 (1992).
- [42] X.Y. Zou, T.P. Grayson, and L. Mandel, *Phys. Rev. Lett.* **69**, 3041 (1992).
- [43] Y.H. Shih, A.V. Sergienko, and M.H. Rubin, *Phys. Rev. A* **47**, 1288 (1993).
- [44] X.Y. Zou, T.P. Grayson, G.A. Barbosa, and L. Mandel, *Phys. Rev. A* **47**, 2293 (1993).
- [45] T.S. Larchuk, R.A. Campos, J.G. Rarity, P.R. Tapster, E. Jakeman, B.E.A. Saleh, and M.C. Teich, *Phys. Rev. Lett.* **70**, 1603 (1993).
- [46] T.J. Herzog, J.G. Rarity, H. Weinfurter, and A. Zeilinger, *Phys. Rev. Lett.* **72**, 629 (1994).
- [47] Y.H. Shih and A.V. Sergienko, *Phys. Lett. A* **186**, 29 (1994).
- [48] T.P. Grayson, J.R. Torgerson, and G.A. Barbosa, *Phys. Rev. A* **49**, 626 (1994).
- [49] Y.H. Shih, A.V. Sergienko, M.H. Rubin, T.E. Kiess, and C.O. Alley, *Phys. Rev. A* **49**, 4243 (1994).
- [50] Y.H. Shih, A.V. Sergienko, M.H. Rubin, T.E. Kiess, and C.O. Alley, *Phys. Rev. A* **50**, 23 (1994).
- [51] Y.H. Shih and A.V. Sergienko, *Phys. Lett. A* **191**, 201 (1994).
- [52] Y.H. Shih and A.V. Sergienko, *Phys. Rev. A* **50**, 2564 (1994).
- [53] A.K. Ekert, J.G. Rarity, P.R. Tapster, and G. Massimo Palma, *Phys. Rev. Lett.* **69**, 1293 (1992).
- [54] A.K. Ekert and G. Massimo Palma, *J. Mod. Opt.* **41**, 2413 (1994).
- [55] J.G. Rarity, P.C.M. Owens, and P.R. Tapster, *J. Mod. Opt.* **41**, 2435 (1994).
- [56] A.V. Sergienko, Y.H. Shih, and M.H. Rubin, *J. Opt. Soc. Am. B* **40**, 859 (1993).
- [57] C.K. Hong, S.R. Friberg, and L. Mandel, *Appl. Opt.* **24**, 3877 (1985).
- [58] A.A. Malygin, A.N. Penin, and A.V. Sergienko [*Dokl. Akad. Nauk SSSR* **281**, 308 (1985) [*Sov. Phys. Dokl.* **30**, 227 (1985)]].
- [59] T.P. Grayson and G.A. Barbosa, *Phys. Rev. A* **49**, 2948 (1994).
- [60] A. Joobeur, B.E.A. Saleh, and M.C. Teich, *Phys. Rev. A* **50**, 3349 (1994).
- [61] P.H.S. Ribeiro, S. Padua, J.C. Machado, and G.A. Barbosa, *Phys. Rev. A* **49**, 4176 (1994).
- [62] P.H.S. Ribeiro, S. Padua, J.C. Machado, and G.A. Barbosa, *Phys. Rev. A* **51**, 1631 (1995).
- [63] D.V. Strekalov, A.V. Sergienko, D.N. Klyshko, and Y.H. Shih, *Phys. Rev. Lett.* **74**, 3600 (1995).
- [64] T.B. Pittman, Y.H. Shih, D.V. Strekalov, and A.V. Sergienko, *Phys. Rev. A* **52**, 3429 (1995).
- [65] A.V. Belinski and D.N. Klyshko, *Zh. Éksp. Teor. Fiz.* **105**, 487 (1994) [*JETP* **78**, 259 (1994)].
- [66] P.W. Milonni and J.H. Eberly, *Lasers* (John Wiley and Sons, New York, 1988).
- [67] M.H. Rubin, D.N. Klyshko, Y.H. Shih, and A.V. Sergienko, *Phys. Rev. A* **50**, 5122 (1994).
- [68] R.J. Glauber, *Phys. Rev.* **130**, 2529 (1963).
- [69] R.J. Glauber, *Phys. Rev.* **131**, 2766 (1963).